Chemical Science

ROYAL SOCIETY OF CHEMISTRY

EDGE ARTICLE

View Article Online
View Journal | View Issue

Cite this: *Chem. Sci.*, 2022, **13**, 8567

All publication charges for this article have been paid for by the Royal Society of Chemistry

Cooperative B–H bond activation: dual site borane activation by redox active κ^2-*N*,*S*-chelated complexes†

Mohammad Zafar,‡[a] Asif Ahmad,‡[a] Suvam Saha,[a] Rongala Ramalakshmi,[a] Thierry Roisnel[b] and Sundargopal Ghosh*[a]

Received 12th February 2022
Accepted 22nd June 2022

DOI: 10.1039/d2sc00907b

rsc.li/chemical-science

Cooperative dual site activation of boranes by redox-active 1,3-*N*,*S*-chelated ruthenium species, *mer*-[$PR_3\{\kappa^2$-*N*,*S*-(L)$\}_2Ru\{\kappa^1$-*S*-(L)$\}$], (*mer*-**2a**: R = Cy, *mer*-**2b**: R = Ph; L = $NC_7H_4S_2$), generated from the aerial oxidation of borate complexes, [$PR_3\{\kappa^2$-*N*,*S*-(L)$\}Ru\{\kappa^3$-*H*,*S*,*S*′-$BH_2(L)_2\}$] (*trans*–*mer*-**1a**: R = Cy, *trans*–*mer*-**1b**: R = Ph; L = $NC_7H_4S_2$), has been investigated. Utilizing the rich electronic behaviour of these 1,3-*N*,*S*-chelated ruthenium species, we have established that a combination of redox-active ligands and metal–ligand cooperativity has a big influence on the multisite borane activation. For example, treatment of *mer*-**2a–b** with BH_3·THF led to the isolation of *fac*-[$PR_3Ru\{\kappa^3$-*H*,*S*,*S*′-$(NH_2BSBH_2N)(S_2C_7H_4)_2\}$] (*fac*-**3a**: R = Cy and *fac*-**3b**: R = Ph) that captured boranes at both sites of the κ^2-*N*,*S*-chelated ruthenacycles. The core structure of *fac*-**3a** and *fac*-**3b** consists of two five-membered ruthenacycles [RuBNCS] which are fused by one butterfly moiety [RuB_2S]. Analogous *fac*-**3c**, [$PPh_3Ru\{\kappa^3$-*H*,*S*,*S*′-$(NH_2BSBH_2N)(SC_5H_4)_2\}$], can also be synthesized from the reaction of BH_3·THF with [$PPh_3\{\kappa^2$-*N*,*S*-$(SNC_5H_4)\}\{\kappa^3$-*H*,*S*,*S*′-$BH_2(SNH_4C_5)_2\}Ru$], *cis*–*fac*-**1c**. In stark contrast, when *mer*-**2b** was treated with BH_2Mes (Mes = 2,4,6-trimethyl phenyl) it led to the formation of *trans*- and *cis*-bis(dihydroborate) complexes [$\{\kappa^3$-*S*,*H*,*H*-$(NH_2BMes)Ru(S_2C_7H_4)\}_2$], (*trans*-**4** and *cis*-**4**). Both the complexes have two five-membered [Ru–$(H)_2$–B–NCS] ruthenacycles with κ^2-H–H coordination modes. Density functional theory (DFT) calculations suggest that the activation of boranes across the dual Ru–N site is more facile than the Ru–S one.

Introduction

Metal–ligand cooperation (MLC) is an important model in catalytic reactions that generates new reactivity patterns in many inorganic/organic transformations.[1,2] Unlike the sole participation of the metal center in classical catalysis, MLC involves a reactive ligand bound to metal that can activate small molecules across the metal–ligand bond, such as, H_2, CO_2, boranes, silanes, alcohols, *etc.*[3–6] Among them, the activation of the B–H bond of boranes along with their catalytic applications in hydroboration became of interest.[7] Metal complexes with polarized M–L bonds (L = O, N, S or C) proved to be very effective for B–H bond activation to yield M–H–B–L species. For example, the M–O bond cooperation (M = Ru or Rh and Ir) can capture H_2BMes or $HBCy_2$ across the metal–oxygen bond.[4c,7b,8] Transition metal complexes with M–S (M = Ru and Fe) or redox non-innocent ligands in combination with MLC can activate BH_3 and 9-BBN molecules.[9,10] For example, ruthenium complexes containing *o*-(*N*-arylamino) thiophenol derivatives show oxidative aromatic ring cleavage in the presence of the superoxide ion (I, Chart 1).[11] Reactions such as hydrogen atom transfer and proton-coupled electron transfer (PCET) reactions that determine the reactivity of H_2 noticeably occurred at the

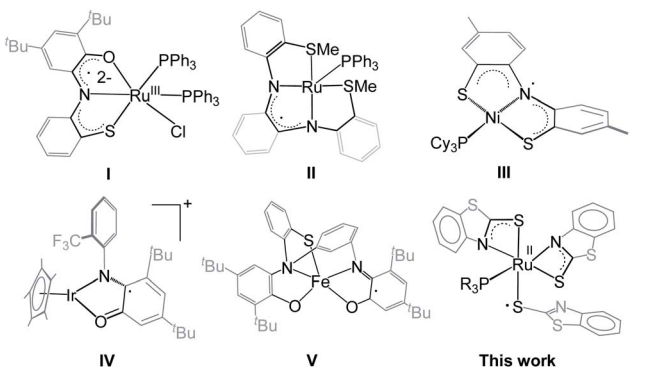

Chart 1 Non-innocent redox-active ligand complexes of various transition metals (I–V).

[a]*Department of Chemistry, Indian Institute of Technology Madras, Chennai 600036, India. E-mail: sghosh@iitm.ac.in*

[b]*Univ of Rennes, CNRS, Institut des Sciences Chimiques de Rennes, UMR 6226, F-35042 Rennes, France*

† Electronic supplementary information (ESI) available. CCDC 1875697, 1984218, 2126931 and 2040802. For ESI and crystallographic data in CIF or other electronic format see https://doi.org/10.1039/d2sc00907b

‡ These authors contributed equally to this work.

redox-active sites of complexes (II–IV, Chart 1).[12,13] On the other hand, for the B–H activation the engagement of MLC with multifunctional reactive sites with redox-active ligands is more useful for accessing key organic transformations.[14]

As part of our current interest in activation of boranes utilizing cooperative reactivity,[15] we have synthesized a number of molybdenum(II) hydroborate species, in which BH_3 is stabilized through Mo–H–B(H_2)–E molybdacycles (E = S, Se or Te).[16] Further, very recently, we have established cooperative Si–H and B–H bond activations by a κ^2-*N*,*S*-chelated borate complex, *trans*–*mer*-**1b** that led to the formation of six-membered ruthenahetero-cycles through hemilabile ring-opening of Ru–N bonds.[17] While working on κ^2-*N*,*S*-chelated species *trans*–*mer*-**1a–b**, we have observed that aerial oxidation of these Ru(II) complexes unusually generates redox-active Ru(III) species, *mer*-**2a–b** that contain dual reactive sites. As a result, we have explored the reactivity of these redox-active Ru(III) species with different types of boranes that demonstrate the synergetic effect of metal and redox active ligands for the activation of boranes.

Results and discussion

As shown in Scheme 1, the room temperature aerial oxidation of Ru(II) borate complexes, *trans*–*mer*-**1a–b** in $CDCl_3$ yielded green Ru(III) complexes, *mer*–**2a–b**. In order to get insight into these reactions, we have monitored the aerial oxidation of one of the molecules **1a** in $CDCl_3$ by $^{11}B\{^1H\}$ NMR that converted to *trans*–*mer*-**2a** after 48 h. The $^{11}B\{^1H\}$ NMR spectrum shows two peaks at $\delta = 19.4$ and -43 ppm that correspond to boric acid [$B(OH)_3$] and the borane adduct [$BH_3 \cdot PCy_3$]. We believe that boric acid (H_3BO_3) has been generated from the aerial oxidation of BH_3 and the [$BH_3 \cdot PCy_3$] adduct has been generated from the reaction of released BH_3 and PCy_3, believed to be produced during the course of the reaction. The ^1H and $^{31}P\{^1H\}$ NMR spectra show broad resonances that suggest the presence of paramagnetic species. The ESI-MS spectra show peaks at *m*/*z* 881.0789 (*mer*-**2a**) and 862.9324 (*mer*-**2b**) with isotopic distribution patterns.

Single crystals for one of these species (*mer*-**2a**) appropriate for XRD analyses were grown from the slow diffusion of a CH_2Cl_2–hexane solution. The geometry of *mer*-**2a** around the Ru center is octahedral (Ma_3b_2c type) comprising two κ^2-1,3-*N*,*S*-chelated rings along with one dangling mercaptobenzo-thiazole

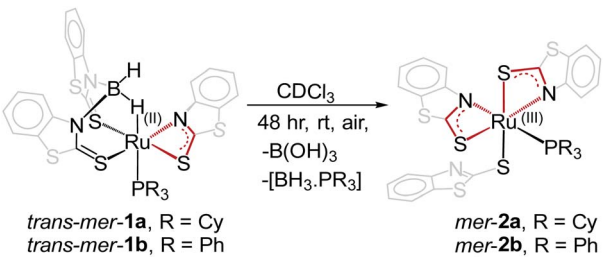

Scheme 1 Conversion of ruthenium(II) borate complexes, *trans*–*mer*-**1a–b** to ruthenium(III) *N*,*S*-chelating mercapto-benzothiazole complexes, *mer*-**2a–b**.

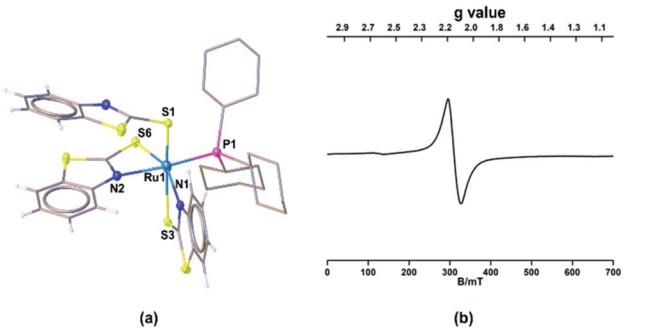

Fig. 1 Molecular structures of *mer*-**2a**. (a) Selected bond lengths (Å) and angles (°): Ru1–P1 2.347(2), Ru1–S1 2.278(2), Ru1–S3 2.491(2), Ru1–S6 2.342(2), Ru1–N1 2.138(6), Ru1–N2 2.164(6); N1–Ru1–S3 66.88(18), N2–Ru1–S6 68.49(18); (b) EPR spectrum of *mer*-**2a**.

and phosphine ligand (Fig. 1a). In the meridional form, the PPh_3 ligand is *trans* to the N atom of one of the κ^2-*N*,*S*-mercaptobenzothiazole donor ligands. The asymmetric unit of *mer*-**2a** possesses a $\pi\cdots\pi$ interaction arising from the overlap of one of the κ^2-*N*,*S*-heterodentate ligands and the dangling one (Fig. S29†). The torsion angles of the four-membered [SCNRu] rings (1.6(6)° and −0.4(6)°) match well with that of *trans*–*mer*-**1a** (0.9(4)°). The Ru–S distances of 2.491(2) and 2.342(2) Å in the four-membered chelate rings are longer as compared to the pendant one (2.278(2) Å).

Further, to understand the nature of these species, the gas phase geometry of *mer*-**2a** was optimized with a doublet spin state by the DFT method with the X-ray coordinates. The computed Ru–P and Ru–S bond lengths were found to be slightly longer than the experimental values (Table S1†). The molecular orbital analysis shows that the unpaired electron typically lies on the orbital with a significant ruthenium d_{yz}-character and a smaller p_y-character of the sulfur atom of the dangling as well as κ^2-*N*,*S*-benzothiazole ligand (SOMO, Fig. 2a). Indeed, the Mulliken spin density for the unpaired electron in *mer*-**2a** is located mostly on the Ru atom (+0.64) with a smaller contribution from the ligated sulfur (+0.20) atom, which is consistent with the spin density plot (Fig. 2b). The Wiberg bond indices (WBI) for Ru–S and Ru–N of 0.771 and 0.340 respectively, suggest two different types of interactions (Table S1†).

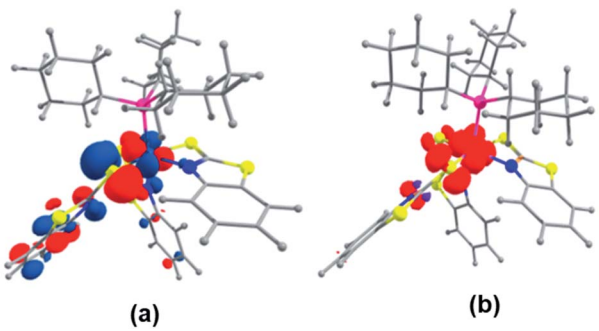

Fig. 2 (a) Calculated SOMO of *mer*-**2a** (isovalue ±0.04 [e $bohr^{-3}]^{1/2}$). (b) A spin density plot for *mer*-**2a** (isovalue 0.004 [e $bohr^{-3}]^{1/2}$).

The solid-state EPR spectra of *mer*-**2a** and *mer*-**2b** at 195 K display signals with the *g* values of 2.116 and 2.118, respectively that confirm the presence of spin delocalization over Ru and the ligand (Fig. 1b and S7†). Although the EPR study confirms the contribution of both [$(L^{-})Ru^{III}$] and [$(L^{\cdot})Ru^{II}$] components to the ground state, the *g* values of 2.116 (*mer*-**2a**) and 2.118 (*mer*-**2b**) differ from that of the organic radical. Note that the typical range of *g* values for Ru^{III} complexes is 2.033–2.205. Thus, this may be due to the distinctive contribution of [$(L_{NCS}^{-})Ru^{III}$] species.[14,18] Although the EPR spectra of any open-shell metal based paramagnetic species typically exhibit rhombohedral signals at low temperature, no observable hyperfine splitting was observed for these species due to the ^{14}N (I = 1) nucleus.[19,20a]

The UV-Vis spectra of *mer*-**2a–b** show a strong absorption band at 240 nm due to the $\pi \rightarrow \pi^*$ transitions and a weak absorption at 430 nm (Fig. S30†). By comparing the UV-Vis spectra of *trans–mer*-**1a** and *mer*-**2a–b**, shown in Fig. S9,† we presume that the broad absorption at 720 nm for *mer*-**2a** and 740 nm for *mer*-**2b** is due to the contribution of the $(L_{NCS}^{\cdot})Ru^{II}$ organic radical in which the ligand has been reduced to the 2-mercaptobenzothiazolate form [$(L_{NCS}^{-})Ru^{III} \leftrightarrow (L_{NCS}^{\cdot})Ru^{II}$]. Note that similar systems describing amido and aminyl radical complexes of Ru(II) have recently been reported by Ghosh and co-workers.[20a] The TD-DFT calculations further suggest that the low energy absorption band for *mer*-**2a** corresponds to the SOMO–LUMO(β) transition (Table S5†). The redox behaviour of both *trans–mer*-**1a** and *mer*-**2a–b** species has further been supported by cyclic voltammetry (CV) studies. The cyclic voltammograms of *mer*-**2a** and *mer*-**2b** in acetonitrile show reversible waves at $E_{1/2} = -0.57$ V, ($I_{pc}/I_{pa} = 0.97$) for *mer*-**2a** and −0.25 V ($I_{pc}/I_{pa} = 0.98$) for *mer*-**2b** (Fig. S8†), which are assigned to the [$Ru^{II}(L^{\cdot})/Ru^{II}(L^{-})$] redox couple.[20a] In addition, the quasi-reversible waves at 0.79 V (*mer*-**2a**) and 0.87 V (*mer*-**2b**) arised due to the Ru^{III}/Ru^{II} redox centered couple.[20]

The redox behaviours of *mer*-**2a** and *mer*-**2b** species were compared with those of other ruthenium complexes containing N_2P_2 or N_2S_2 ligands derived from *o*-phenylenediamine. For example, Mascharak and co-workers reported the cyclic voltammogram of [*cis*-(dppQ)$RuCl_2$] (dppQ = 1,2-bis-*N*-[2′(diphenylphosphanyl) benzoyl]benzoquinonediimine) that shows two reversible redox events at −0.28 and 0.90 V *versus* Fc^{+}/Fc and an irreversible event at −1.35 V.[20c] The irreversible feature at −1.35 V was assigned to the ligand-centered reduction of the *o*-diiminosemi-quinone radical to a fully reduced *o*-phenylenediamine unit. The reversible wave at −0.28 V was assigned to the second ligand-centered redox event, and the reversible wave at 0.90 V was assigned to the Ru^{III}/Ru^{II} redox couple. Similarly, Daly and co-workers reported two reversible redox events at −0.78 V and −0.28 V *versus* Fc^{+}/Fc (Ru^{II}/Ru^{I} and Ru^{III}/Ru^{II} redox couples) and irreversible features at −2.46 V as the ligand centered redox event.[12] Therefore, based on the above results, the additional irreversible half-wave potentials, appearing at 0.46 V (*mer*-**2a**) and 0.54 V (*mer*-**2b**), have been assigned to the oxidation of the second *N*,*S*-donor mercapto-benzothiazolyl ligand.[20e] Nonetheless, to gain further insight into the nature of the half-wave potentials of these complexes, we performed the molecular orbital analysis of the oxidised form of *mer*-**2a** and *mer*-**2b** that shows mixing of orbitals between Ru–metal and the heterocyclic ligand (Fig. S39†). Thus, based on the DFT calculations, the assignments of the redox couples as ligand or metal-centered oxidation are unclear. We have also recorded the current *vs.* square root of scan rate for one of the molecules *mer*-**2a** and the corresponding plot (current *vs.* square root of scan rate) is provided in the revised ESI (Fig. S31–S33†). Note that the redox couple observed at −0.57 V shows reversible wave linearity with increasing scan rate (Fig. S32†). However, the peak current at 0.79 V is not proportional to the square root of scan rate and thus, it may be considered as a quasi-reversible wave. The peak current at 0.46 V shows an irreversible half wave.

The presence of dual reactive sites and the redox active hemilabile κ^2-1,3-*N*,*S*-bidentate chelate ligands in *mer*-**2a–b** encouraged us to study their reactivity with various boranes. As a result, we treated these species with an excess of $BH_3 \cdot THF$ that resulted in the formation of yellow **3a** and **3b** with 38% and 42% yields, respectively (Scheme 2). Both the complexes were characterized by ^1H and $^{13}C\{^1H\}$ NMR, IR spectroscopy, and single crystal X-ray diffraction studies. The $^{11}B\{^1H\}$ NMR spectra of both the complexes feature a single resonance at δ −11.5 and δ −10.1 ppm, respectively for **3a** and **3b**. The ^1H NMR spectra show the presence of the mercaptobenzothiazole ligand in the region of δ 7.87–7.26 ppm. In addition, two broad resonances, appearing at δ 2.97 and −14.43 ppm for **3a** and 3.01 and −13.24 ppm for **3b**, have been assigned to B–H and Ru–H–B hydrides. The broad ^1H chemical shifts were resolved into a doublet and an apparent triplet upon ^{11}B decoupling ($^2J_{HP} = 14.1$ Hz, $^2J_{HH} = 14.1$ Hz (**3a**); and $^2J_{HP} = 12.0$ Hz, $^2J_{HH} = 12.0$ Hz (**3b**). These NMR signatures indirectly ensure that the hydride is *cis* oriented to the phosphine ligand. The $^{31}P\{^1H\}$ NMR revealed a singlet at δ 71.0 for **3a** and 60.9 ppm for **3b**. The mass spectra showed a molecular ion peak at *m*/*z* 772.1165 for **3a** and 776.9636 for **3b**. Based on all the spectroscopic data along with mass spectrometric data, it was clear that both the species are diamagnetic. However, a clear explanation eluded us until the single-crystal X-ray diffraction analysis of one of these species **3a** was performed.

The solid-state X-ray structure of **3a**, shown in Fig. 3a, displays a symmetrical structure with C_s symmetry, wherein the

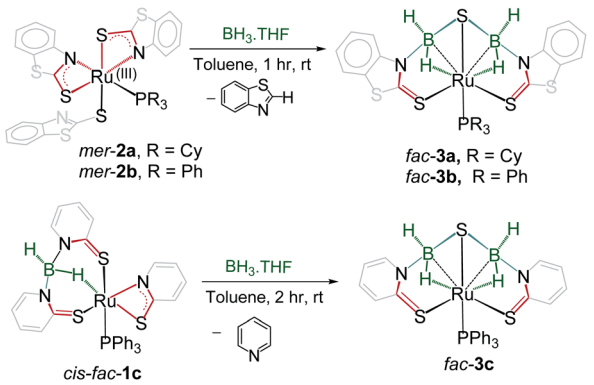

Scheme 2 Reactivity of *mer*-**2a–b** and *cis–fac*-**1c** with $BH_3 \cdot THF$.

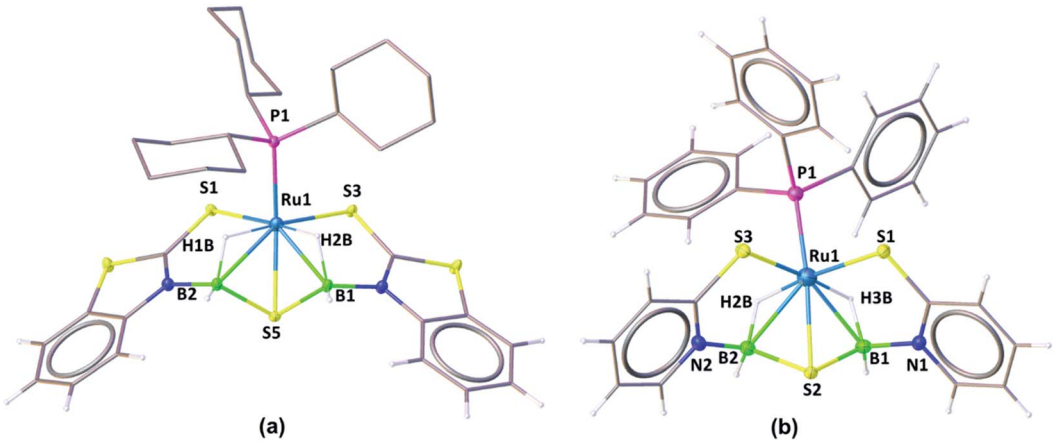

Fig. 3 Molecular structures of *fac*-**3a** (a) and *fac*-**3c** (b). Selected bond lengths (Å) and angles (°): *fac*-**3a** (a) Ru1–B2 2.276(2), Ru1–B1 2.293(3), Ru1–P1 2.307(6), Ru1–S1 2.384(6), Ru1–S3 2.383(6), Ru1–S5 2.4184(6), Ru1–H1B 1.69(3), Ru1–H2B 1.69(3), B2–Ru1–B1 75.66(9), B2–Ru1–S5 48.08(7); *fac*-**3c** (b) Ru1–B2 2.285(4), Ru1–B1 2.281(4), Ru1–P1 2.2830(9), Ru1–S1 2.3611(8), Ru1–S3 2.3535(9), Ru1–S2 2.4090(9), Ru1–H2B 1.63(3), Ru1–H3B 1.66(3), B2–Ru1–B1 77.74(14), B2–Ru1–S5 48.17(10).

mirror plane of symmetry passed through the S5–Ru1–P1. The ruthenium center adopts an octahedral geometry in the facial form in which the phosphine ligand is present in *trans* to the sulfur atom. Thus, we believe that complex **3a**, now *fac*-**3a**, is generated from the insertion of two BH_2 moieties across the initial Ru–N bonds of κ^2-*N*,*S*-chelated heterocycles. The S atom in the butterfly core is presumably generated from the C–S bond cleavage of the pendant mercaptobenzothiazole ligand. To validate this concept, we have monitored the reaction of *mer*-**2a** with $BH_3\cdot$THF by $^{13}C\{^1H\}$ and ^1H NMR spectroscopy in toluene-d_8. The $^{13}C\{^1H\}$ NMR spectrum (after 2 h) shows chemical shifts in the range of δ = 149–134 ppm that correspond to the benzothiazole ligand. On the other hand, the ^1H chemical shift at δ = 9.4 ppm corresponds to the C–H proton of the benzothiazole ligand.[21] Thus, we firmly believe that the source of sulphide for the formation of **3a** or **3b** is the mercapto-benzothiazole ligand. Note that recently Wang and co-workers reported a similar type of reaction that yielded the Mo(II)hydride complex, [Cp*MoH(1,2-$Ph_2PC_6H_4SBH_2$)] in which a BH_2 moiety is coordinated with the Mo–S bond.[22] The BH_2 moieties in *fac*-**3a** and *fac*-**3b** are further stabilized by one sulfur atom (S5, *fac*-**3a**), generating two unique five-membered RuBNCS ruthenacycles, which are fused by one {RuB_2S} butterfly unit. The average Ru–B distance (2.284 Å) in *fac*-**3a** is comparable with the bond lengths of 2.266(8) Å and 2.216(6) Å observed in [$RuH(PCy_3)_2$\{(μ-H)$_2$-$BMeCH_2SMe$\}][23] and [Cp*Ru(μ-H)$_2$B($NC_7H_4S_2$)],[24] respectively. Similarly, the average B–S bond distance of 1.917 Å is consistent with borane–thiolate species that typically fall in the range of 1.949–1.911 Å.[25] The DFT analysis further established that the borane activation across the Ru–N bond is more favourable than the Ru–S bond with a lower energy of 50.2 kcal mol^{-1}. This has also been supported by NBO analysis, where the Wiberg bond index of Ru–S (0.771) is significantly stronger than that of Ru–N (0.340) (Table S1†).

The meridional and facial orientations of all the complexes have been assigned largely based on the coordination of hydride and phosphine ligands to metal. The coordination modes were established in comparison with the J_{PH} coupling constants of similar molecules.[14,23,26a] For example, the ^1H NMR spectrum of *trans–mer*-**1b** shows a broad hydride peak at δ = −3.71 ppm that converted to a doublet of doublet upon ^{11}B decoupling ($^2J_{HP}$ = 33.1 Hz, $^2J_{HH}$ = 16.4 Hz). This indirectly suggests that the hydride is *trans* to the phosphine ligand, and all mercaptobenzothiazole sulfurs are arranged in the meridional fashion (Fig. S10†). However, in facial-orientation, the broad hydride peak at δ = −13.24 ppm transformed to an apparent triplet with coupling constants $^2J_{HP}$ = 12.0 Hz and $^2J_{HH}$ = 12.0 Hz. This is due to the presence of the adjacent *cis*-oriented phosphine group in which the mercaptobenzothiazolyl sulfur coordinated facially.[26b,c]

Note that analogous *fac*-**3c**, [PPh_3Ru{κ^3-*H*,*S*,*S*′-(NH_2BSBH_2N)(SC_5H_4)$_2$}] was synthesized as a yellow crystalline solid from the room temperature reaction of [{κ^3-*H*,*S*,*S*′-$H_2B(SNC_5H_4)_2$}Ru{κ^2-*N*,*S*-(SNC_5H_4)}PPh_3],[27] *cis–fac*-**1c** and $BH_3\cdot$THF (Scheme 2). Complex *fac*-**3c** was characterized by comparing its spectroscopic data with the mass spectrometric data of *fac*-**3a–b** that show a molecular ion peak at 642.0321, and a solid-state X-ray diffraction analysis. The $^{11}B\{^1H\}$ NMR spectrum shows a sharp peak in the upfield region δ = −3.8 ppm. The ^1H NMR spectrum of *fac*-**3c** displayed an upfield resonance at δ = −12.27 ppm due to the Ru–H–B proton. This broad ^1H chemical shift was resolved into an apparent triplet upon ^{11}B decoupling with coupling constants $^2J_{HP}$ = 13.1 Hz and $^2J_{HH}$ = 13.1 Hz. The solid-state X-ray structure of *fac*-**3c**, shown in Fig. 3b, shows a butterfly core containing the S atom similar to that of *fac*-**3a**. The S atom in the butterfly core has presumably been generated from the C–S bond cleavage of the pendant mercaptopyridyl ligand. Further, to get some insight into the reaction intermediates, we have monitored the reaction of *cis–fac*-**1c** with $BH_3\cdot$THF using ^1H and ^{13}C NMR in toluene-d_8. The $^{13}C\{^1H\}$ NMR spectrum (after 2 h) shows chemical shifts in the range of δ = 134–148.6 ppm that correspond to free pyridine. On the other

hand, the ^{1}H chemical shift at $\delta = 8.68$ ppm corresponds to the C–H proton of the pyridine ligand.[28]

To have a further understanding of the MLC binding effect in 1,3-*N*,*S*-chelated ruthenium complexes, the electrochemistry of *fac*-**3a–b** was studied (Fig. S8†). The single quasi-reversible redox observed at $E_{1/2} = 0.59$ V (*fac*-**3a**) and 0.62 V (*fac*-**3b**) assigned to the Ru^{III}/Ru^{II} redox couple indicates that the MLC reduces the electrochemical activity of *fac*-**3a–b** when compared with *trans–mer*-**1a–b** and *mer*-**2a–b** species. As there exists no equilibrium between *fac*-**3a–b** and *mer*-**2a–b** under an applied potential (loss of BH_3), we believe that the cooperativity with two BH_3 units in *fac*-**3a–b** is stronger as compared to *trans–mer*-**1a–b**.

The NBO and QTAIM analyses show the coordination of BH_2 with S and Ru atoms. As shown in Fig. 4a–d, it is evident that one of the B–H bonds donates electron density to the Ru center and the S donates a lone pair of electrons to Ru. This was further supported by natural charge analysis that indicates positive natural charges both at S and B atoms ($q_B = 0.029$, $q_S = 0.026$). Thus, it is apparent that S and B act as donors and the Ru center ($q_{Ru} = -0.429$) can be considered as an acceptor. The Wiberg bond indices (WBI) of 0.984 and 0.979 with regard to B1–S5 and B2–S5 bonds support strong bonding interactions. The HOMO−2 of *fac*-**3a**, shown in Fig. 4c, suggests that the electron density is mostly localized on the B–S–B moiety and Ru center. Further, topology analysis of *fac*-**3a** reveals the presence of B–S, B–H, Ru–H and Ru–S bond critical points (BCPs) and ring critical points (RCPs). The topological features at BCPs of Ru–H, Ru–S and Ru–P bonds are characterized as dative interactions (Fig. 4d and Table S4†).

With the conditions for the formation of *fac*-**3a–c** in hand, reactivity of *mer*-**2a–b** with bulky borane such as mesityl borane

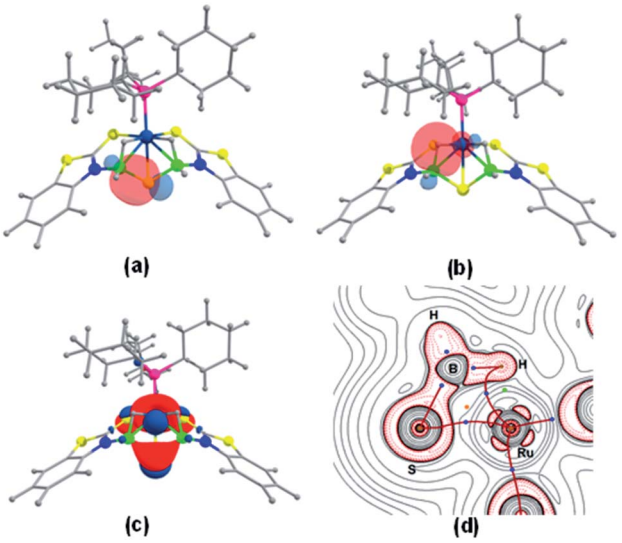

Fig. 4 Natural bond orbital interaction between the B–S bond (a) and the B–H–Ru bond (b) in *fac*-**3a** (isovalue ±0.04 [e bohr^{-3}]$^{1/2}$); (c) HOMO−2 of *fac*-**3a**; (d) contour-line map of the Laplacian of the electron density in the Ru–S–H plane of *fac*-**3a**. BCPs and RCPs correspond to blue and orange dots and red lines indicate bond paths.

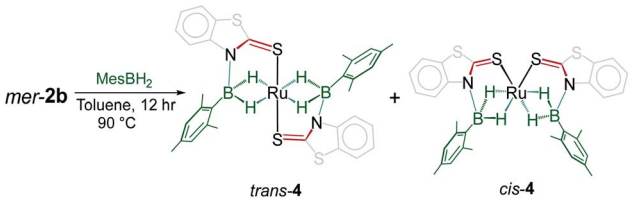

Scheme 3 Reactivity of *mer*-**2b** with mesityl borane.

(H_2BMes) became of interest. Although the reaction of *mer*-**2a** with H_2BMes resulted in decomposition of the starting material over time, mild thermolysis of *mer*-**2b** with a stoichiometric amount of mesityl borane in toluene resulted in the formation of complex **4**. Thin-layer chromatographic workup allowed us to isolate pure **4** as a yellow crystalline solid in 45% yield, which was characterized by multinuclear NMR and IR spectroscopic methods (Scheme 3). The $^{11}B\{^1H\}$ NMR spectrum of **4** shows two broad resonances at δ 39.4 and 31.2 ppm. In addition to ^{1}H chemical shifts for the mercaptobenzo-thiazolyl ligand, the ^{1}H NMR spectrum of **4** shows three up-field chemical shifts at δ −11.42, −10.41 and −10.01 ppm. The mass spectrum shows a molecular ion peak at *m*/*z* 698.0799. The $^{31}P\{^1H\}$ NMR shows the presence of no ^{31}P chemical shift. All the spectroscopic data along with mass spectrometric data suggest **4** as a mixture of two Ru−borate species. However, the identity was unclear until an X-ray crystallographic analysis was carried out for one of them.

A slow evaporation of a CH_2Cl_2/hexane solution of **4** at −5 °C yielded two different types of crystals. The X-ray diffraction analysis was performed on a yellow crystal which was manually picked up from the Schlenk tube. The solid-state X-ray structure of this yellow crystal, shown in Fig. 5, shows a distorted-octahedral geometry in which four hydrogen atoms are placed in a square plane and two S atoms occupy the axial positions. This clearly shows that two units of H_2BMes have been inserted into two Ru–N bonds of κ^2-*N*,*S*-chelated ligands of *mer*-**2b** resulting

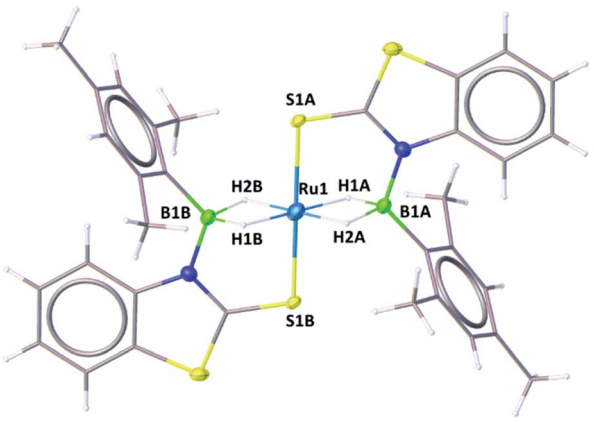

Fig. 5 Molecular structures of *trans*-**4**. Selected bond lengths (Å) and angles (°): Ru1–B1A 2.172(4), Ru1–S1A 2.3221(10), B1–N1 1.542(5), B1–C1 1.580(5), B1–Ru1–B1 180.0(2), B1–Ru1–S1 95.86(11), S1–Ru1–S1 180.0, C1–B1–Ru1 127.2(3).

in the formation of two five-membered Ru–B–NCS ruthenacycles. Interestingly, the geometry of this crystal has an inversion center on Ru. Thus, this molecule can be defined as *trans*-[Ru{κ^3-*S*,*H*,*H*-(NBH$_2$Mes)(S$_2$C$_7$H$_4$)}$_2$] (*trans*-**4**).

Although we failed to get single crystals for the other species, all the spectroscopic data and mass spectrometric data clearly suggest the presence of both *trans*-**4** and *cis*-**4** species. For the *trans*-**4** isomer (C_{2h} symmetry) the ^{11}B chemical shift at $\delta = 39.4$ ppm has been assigned to two equivalents of boron atoms and the ^{1}H chemical shift at $\delta = -11.42$ ppm has been assigned to four Ru–H–B protons which are in an equivalent environment. However, for the *cis*-**4** (C_{2V} symmetry), the ^{11}B chemical shift at $\delta = 31.2$ ppm is due to the presence of two equivalents of boron. The two broad ^{1}H chemical shifts at $\delta = -10.41$ and $\delta = -10.01$ ppm for the Ru–H–B protons emanate from the presence of two different groups opposite to the hydrogen atom. Two Ru–H–B protons are *trans* to mercaptobenzothiazolyl sulphur and other two Ru–H–B protons are *trans* to each other (Fig. S26†).

As listed in Table 1, the Ru–B distance of 2.172(4) Å for *trans*-**4** is consistent with that of the bis(dihydroborate) complex, Ru[(μ-H)$_2$ BC$_8$H$_{14}$]$_2$(PCy$_3$)[29] (2.160(2) Å) and other reported dihydroborate species.[29–33] The Ru–B distances in *trans*-**4** fall in the range of 2.103(2)–2.266(8) Å,[15] which are significantly longer as compared to those of σ-borane complexes, for example,

Table 1 Selected spectroscopic and structural parameters of transition metal bis-(dihydroborate) complexes and *cis*-**4** and *trans*-**4**

	Spectroscopic parameters (ppm)		Structural parameters (Å)		
Bis-(dihydroborate)	^{1}H(Ru–H)	^{11}B{^{1}H}	*d*[M–B]	*d*[M–H]	Ref.
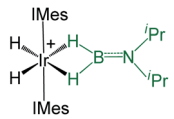	−15.50, −5.83	37.9	2.088(5)	1.85(12)	29a
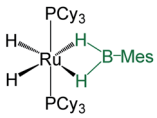	−11.26, −6.10	58.0	1.938(4)	1.61(3), 1.59(3), 1.73(3), 1.77(3)	29b
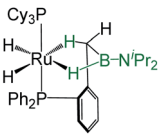	−13.22, −8.58, −6.71, −1.00	35.5	2.173(3)	1.59(3), 1.69(3), 1.49(3), 1.97(3)	33
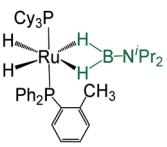	−11.58, −6.29	46.0	—	—	33
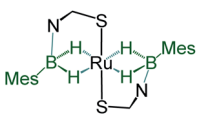	−11.42	39.4	2.172(4)	1.60(4), 1.62(4)	This work
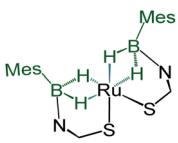	−10.41, −10.01	31.2	—	—	This work
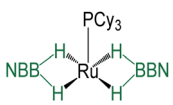	−12.43	58.8	2.160(2), 2.085(2)	1.63(2), 1.66(2), 1.60(2), 1.63(2)	30
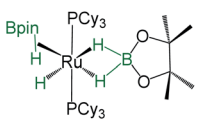	−11.4, −8.03, −7.13	37.3	2.157(5), 2.188(5)	1.48(3), 1.58(3), 1.49(3), 1.55(3)	31
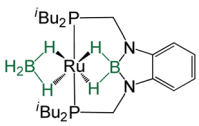	−14.57, −5.78	11.9, 40.8	2.048(9), 2.333(9)	1.615, 1.629, 1.843, 1.860	32

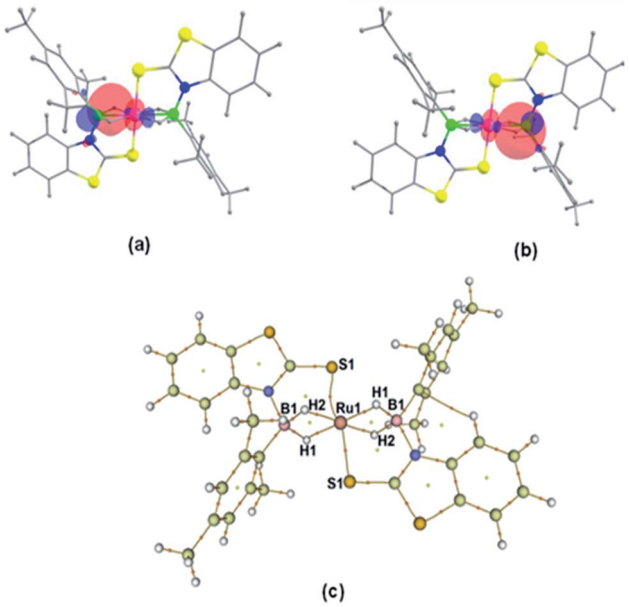

Fig. 6 (a and b) Donor–acceptor interaction between B–H and the Ru atom obtained by NBO analysis of *trans*-**4**. (c) QTAIM analysis of *trans*-**4**. Bond paths are indicated by yellow lines and BCPs and RCPs are represented by orange and yellow dots respectively.

$[Ru(PCy_3)_2(H)_2(BH_2Mes)]$[29b] (1.938(4) Å) and $[Cp^*Ru(P^iPr_3)(BH_2Mes)]B(C_6F_5)_4$ (ref. 34) (1.921(2) Å). The B1–Ru1–B1 angle of 180.0(2)° shows a perfect symmetrical coordination of borane to the metal center, unlike tetrahydroborate species, [PBP](μ-$H)_2Ru(\eta^2\text{-}BH_4)$][32] (177.4(4)°) and $Ru[(\mu\text{-}H)_2BC_8H_{14}]_2(PCy_3)$[30] (147.68(8)°). The WBI of 0.369 for the Ru–B bonds of *trans*-**4** also supports symmetrical interaction (Table S1†). The analysis further suggests that the *trans*-isomer is thermodynamically more stable in which the relative total energy for the *trans*-4 isomer is 0.46 kcal mol^{-1} lower than that of the *cis*-4 isomer. The donor–acceptor interaction between the B–H bond and Ru is confirmed by second-order perturbation analysis with a stabilization energy of 11.34 kcal mol^{-1} (Fig. 6a and b). Although the QTAIM analysis shows all the BCPs in *trans*-**4**, it can't identify the interaction between Ru and B (Fig. 6c).[35]

Although mesityl borane, H_2BMes, has been accessible since 1994,[36] structurally characterized species, other than borylene complexes, are very limited.[37] For example, the first ruthenium terminal borylene complex, $[Ru(BMes)(PCy_3)_2]$, was synthesized by double B–H activation of H_2BMes.[37a] Recently, Hayes and co-workers have isolated and structurally characterized the Rh–borylene complex[37b] from the rhodium pincer complex, $[(^{iPr}NNN)Rh(CO)]$ (^{iPr}NNN = 2,5-$[^iPr_2P{=}N(4\text{-}^iPrC_6H_4)]_2$-$N(C_4H_2)^-$]) and H_2B–Mes by reversible dehydrogenation of H_2BMes. Interestingly, not many examples are known where the addition of H_2BMes occurred in a κ^2-coordination fashion into the polar M–L bonds.[7b,17,38] Some of the dihydroborate species, for example, $[Cp^*Ru(\kappa^3\text{-}P,H,H\text{-}(^iPr)P(C_9H_6O\text{–}H_2BMes)]$[38] and [M $\{\kappa^3\text{-}N,H,H\text{-Xyl}(N)P(OH_2\ BMes)(OEt)_2\}(\eta^4\text{-COD})]$ (M = Rh and Ir),[7b] have been isolated from the insertion of H_2BMes into the corresponding M–O bonds. The first bis(σ-borane) species, $[Ru(PCy_3)_2(H)_2\ (\eta^2\text{:}\eta^2\text{-}BH_2Mes)]$, was reported by Sabo-Etienne and Alcaraz, isolated from the reaction of H_2BMes and $[RuH_2(PCy_3)_2(\eta^2\text{-}H_2)_2]$.[29b]

Conclusions

In summary, we have developed some redox-active complexes supported by hemilabile κ^2-*N*,*S*-chelated ruthena-cycles that undergo unusual dual site B–H bond activation with free and bulky boranes. When the reaction was carried out with free borane, one of the B–H bonds of the BH_3 unit cleaved and the rest of the BH_2 moiety was captured by the Ru–N bond that led to two five-membered (RuBNCS) ruthenacycles. In contrast, bulky borane mesitylborane generated *trans* and *cis* species, in which two H_2BMes units are coordinated to the Ru center. A combined experimental and theoretical study shows that a combination of redox-active ligands and metal–ligand cooperativity has a major role in multisite borane activation for smaller and bulky boranes.

Data availability

Crystallographic data have been deposited with the Cambridge Crystallographic Data Center as supplementary publication no CCDC-1875697 (*mer*-**2a**), CCDC-1984218 (*fac*-**3a**), CCDC-2126931 (*fac*-**3c**), CCDC-2040802 (*trans*-**4**). These data can be obtained free of charge from The Cambridge Crystallographic Data Centre *via* **https://www.ccdc.cam.ac.uk/data_request/cif**.

Author contributions

M. Zafar, A. Ahmad and S. Saha have executed the experimental synthesis, characterization, and analysis of the data. R. Ramalakshmi has conducted the theoretical calculations. All authors have contributed to the preparation of the manuscript. S. Ghosh has supervised the project.

Conflicts of interest

There are no conflicts to declare.

Acknowledgements

This research was funded by CEFIPRA, grant number 5905-1. DST-FIST, India. M. Z. thanks IIT Madras for a research fellowship. A. A. thanks the Council of Scientific & Industrial Research (CSIR) for a research fellowship. S. S. thanks INSPIRE for a research fellowship. R. R. thanks the University Grant Commission (UGC), India, for the research fellowship.

Notes and references

1 (*a*) R. Peters, *Cooperative Catalysis*, Wiley-VCH, Weinheim, 2015; (*b*) L. Omann, C. D. F. Konigs, H. F. T. Klare and M. Oestreich, *Acc. Chem. Res.*, 2017, **50**, 1258–1269; (*c*) K.-S. Feichtner and V. H. Gessner, *Chem. Commun.*, 2018, **54**, 6540–6553.

2 (*a*) T. Higashi, S. Kusumoto and K. Nozaki, *Chem. Rev.*, 2019, **119**, 10393–10402; (*b*) H. Li, T. P. Goncalves, D. Lupp and K.-W. Huang, *ACS Catal.*, 2019, **9**, 1619–1629; (*c*) E. R. M. Habraken, A. R. Jupp, M. B. Brands, M. Nieger, A. W. Ehlers and J. C. Slootweg, *Eur. J. Inorg. Chem.*, 2019, **2019**, 2436–2442; (*d*) M. R. Elsby and R. T. Baker, *Chem. Soc. Rev.*, 2020, **49**, 8933–8987.

3 (*a*) C. Gunanathan and D. Milstein, *Acc. Chem. Res.*, 2011, **44**, 588–602; (*b*) R. H. Morris, *Acc. Chem. Res.*, 2015, **48**, 1494–1502.

4 (*a*) C. C. Comanescu and V. M. Iluc, *Chem. Commun.*, 2016, **52**, 9048–9051; (*b*) J. Y. Corey, *Chem. Rev.*, 2016, **116**, 11291–11435; (*c*) L. T. Scharf, J. Weismann, K.-S. Feichtner, F. Lindl and V. H. Gessner, *Chem.–Eur. J.*, 2018, **24**, 3439–3443.

5 (*a*) R. Stichauer, A. Helmers, J. Bremer, M. Rohdenburg, A. Wark, E. Lork and M. Vogt, *Organometallics*, 2017, **36**, 839–848; (*b*) C. Erken, A. Kaithal, S. Sen, T. Weyhermüller, M. Hölscher, C. Werle and W. Leitner, *Nat. Commun.*, 2018, **9**, 4521; (*c*) I. Heuermann, B. Heitmann, R. Stichauer, D. Duvinage and M. Vogt, *Organometallics*, 2019, **38**, 1787–1799.

6 (*a*) S. P. Cronin, J. M. Strain, M. S. Mashuta, J. M. Spurgeon, R. M. Buchanan and C. A. Grapperhaus, *Inorg. Chem.*, 2020, **59**, 4835–4841; (*b*) R. Stichauer and M. Vogt, *Organometallics*, 2018, **37**, 3639–3643.

7 (*a*) J. B. Geri and N. K. Szymczak, *J. Am. Chem. Soc.*, 2015, **137**, 12808–12814; (*b*) M. W. Drover, L. L. Schafer and J. A. Love, *Angew. Chem.*, 2016, **128**, 3233–3238; *Angew. Chem., Int. Ed.*, 2016, **55**, 3181–3186; (*c*) M. Ito, M. Itazaki and H. Nakazawa, *Inorg. Chem.*, 2017, **56**, 13709–13714; (*d*) J. W. Nugent, M. G. Melchor and A. R. Fout, *Organometallics*, 2020, **39**, 2917–2927; (*e*) X. Zhai, M. Pang, L. Feng, J. Jia, C.-H. Tung and W. Wang, *Chem. Sci.*, 2021, **12**, 2885–2889.

8 M. A. Rankin, K. D. Hesp, G. Schatte, R. McDonald and M. Stradiotto, *Dalton Trans.*, 2009, 4756–4765.

9 (*a*) T. Stahl, K. Mether, Y. Ohki, K. Tatsumi and M. Oestreich, *J. Am. Chem. Soc.*, 2013, **135**, 10978–10981; (*b*) H. Song, K. Ye, P. Geng, X. Han, R.-Z. Liao, C.-H. Tung and W. Wang, *ACS Catal.*, 2017, **7**, 7709–7717.

10 V. Lyaskovskyy and B. Bruin, *ACS Catal.*, 2012, **2**, 270–279.

11 S. Maity, S. Kundu, S. Mondal, S. Bera and P. Ghosh, *Inorg. Chem.*, 2017, **56**, 3363–3376.

12 (*a*) G. Durgaprasad, J. A. Luna, K. D. Spielvogel, C. Haas, S. K. Shaw and S. R. Daly, *Organometallics*, 2017, **36**, 4020–4031; (*b*) K. E. Rosenkoetter, M. K. Wojnar, B. J. Charette, J. W. Ziller and A. F. Heyduk, *Inorg. Chem.*, 2018, **57**, 9728–9737; (*c*) M. R. Ringenberg, S. L. Kokatam, Z. M. Heiden and T. B. Rauchfuss, *J. Am. Chem. Soc.*, 2008, **130**, 788–789.

13 (*a*) J. I. van der Vlugt, *Chem.–Eur. J.*, 2019, **25**, 2651–2662; (*b*) L. Alig, M. Fritz and S. Schneider, *Chem. Rev.*, 2019, **119**, 2681–2751; (*c*) D. R. Weinberg, C. J. Gagliardi, J. F. Hull, C. F. Murphy, C. A. Kent, B. C. Westlake, A. Paul, D. H. Ess, D. G. McCafferty and T. J. Meyer, *Chem. Rev.*, 2012, **112**, 4016–4093.

14 K. D. Spielvogel, J. A. Luna, S. M. Loria, L. P. Weisburn, N. C. Stumme, M. R. Ringenberg, G. Durgaprasad, J. M. Keith, S. K. Shaw and S. R. Daly, *Inorg. Chem.*, 2020, **59**, 10845–10853.

15 K. Saha, D. K. Roy, R. D. Dewhurst, S. Ghosh and H. Braunschweig, *Acc. Chem. Res.*, 2021, **54**, 1260–1273.

16 R. Ramalakshmi, K. Saha, D. K. Roy, B. Varghese, A. K. Phukan and S. Ghosh, *Chem.–Eur. J.*, 2015, **21**, 17191–17195.

17 M. Zafar, R. Ramalakshmi, A. Ahmad, P. K. S. Antharjanam, S. Bontemps, S. Sabo-Etienne and S. Ghosh, *Inorg. Chem.*, 2021, **60**, 1183–1194.

18 M. M. T. Khan, D. Srinivas, R. I. Kureshy and N. H. Khan, *Inorg. Chem.*, 1990, **29**, 2320–2326.

19 M. Chatterjee, S. Mondal, P. Ghosh, W. Kaim and G. K. Lahiri, *Inorg. Chem.*, 2018, **57**, 12187–12194.

20 (*a*) S. Kundu, D. Dutta, S. Maity, T. Weyhermüller and P. Ghosh, *Inorg. Chem.*, 2018, **57**, 11948–11960; (*b*) N. P. V. Leest, M. A. Tepaske, J. H. Oudsen, B. Venderbosch, N. R. Rietdijk, M. A. Siegler, M. Tromp, J. I. V. D. Vlugt and B. D. Bruin, *J. Am. Chem. Soc.*, 2020, **142**, 552–563; (*c*) N. L. Fry, M. J. Rose, C. Nyitray and P. K. Mascharak, *Inorg. Chem.*, 2008, **47**, 11604–11610; (*d*) H. Masui, A. B. P. Lever and P. R. Auburn, *Inorg. Chem.*, 1991, **30**, 2402–2410; (*e*) S. D. J. McKinnon, B. O. Patrick, A. B. P. Lever and R. G. Hicks, *Chem. Commun.*, 2010, **46**, 773–775.

21 (*a*) D. A. Lomov, Y. M. Yutilov and N. N. Smolyar, *Russ. J. Org. Chem.*, 2006, **42**, 241–242; (*b*) T. Itoh and T. Mase, *Org. Lett.*, 2007, **9**(18), 3687–3689.

22 S.-F. Hou, J.-Y. Chen, M. Xue, M. Jia, X. Zhai, R.-Z. Liao, C.-H. Tung and W. Wang, *ACS Catal.*, 2020, **10**, 380–390.

23 Y. Gloaguen, G. Alcaraz, A.-F. Péharman, E. Clot, L. Vendier and S. Sabo-Etienne, *Angew. Chem.*, 2009, **121**, 3008–3012; *Angew. Chem., Int. Ed.*, 2009, **48**, 2964–2968.

24 R. S. Anju, D. K. Roy, B. Mondal, K. Yuvaraj, C. Arivazhagan, K. Saha, B. Varghese and S. Ghosh, *Angew. Chem.*, 2014, **126**, 2917–2921; *Angew. Chem., Int. Ed.*, 2014, **53**, 2873–2877.

25 K. Saha, U. Kaur, S. Kar, B. Mondal, B. Joseph, P. K. S. Antharjanam and S. Ghosh, *Inorg. Chem.*, 2019, **58**, 2346–2353.

26 (*a*) G. Alcaraz, L. Vendier, E. Clot and S. Sabo-Etienne, *Angew. Chem., Int. Ed.*, 2010, **49**, 918–920; (*b*) R. Adam, E. Alberico, W. Baumann, H. Drexler, R. Jackstell, H.-J. Junge and M. Beller, *Chem.–Eur. J.*, 2016, **22**, 4991–5002; (*c*) D. Y. Shopov, B. Rudshteyn, J. Campos, V. S. Batista, R. H. Crabtree and G. W. Brudvig, *J. Am. Chem. Soc.*, 2015, **137**, 7243–7250.

27 M. Zafar, R. Ramalakshmi, K. Pathak, A. Ahmad, T. Roisnel and S. Ghosh, *Chem.–Eur. J.*, 2019, **25**, 13537–13546.

28 B. Jiang, J. Jia, Y. Sun, Y. Wang, J. Zeng, X. Bu, L. Shi and X. Sun Xiaobo Yang, *Chem. Commun.*, 2020, **56**, 13389–13392.

29 (*a*) C. Y. Tang, A. L. Thompson and S. Aldridge, *Angew. Chem.*, 2010, **122**, 933–937; *Angew. Chem., Int. Ed.*, 2010, **49**, 921–925; (*b*) G. Alcaraz, E. Clot, U. Hemstedt,

L. Vendier and S. Sabo-Etienne, *J. Am. Chem. Soc.*, 2007, **129**, 8704–8705.

30 K. Essalah, J.-C. Barthelat, V. Montiel, S. Lachaize, B. Donnadieu, B. Chaudret and S. Sabo-Etienne, *J. Organomet. Chem.*, 2003, **680**, 182–187.

31 V. Montiel-Palma, M. Lumbierres, B. Donnadieu, S. Sabo-Etienne and B. Chaudret, *J. Am. Chem. Soc.*, 2002, **124**, 5624–5625.

32 T. Miyada, E. H. Kwan and M. Yamashita, *Organometallics*, 2014, **33**, 6760–6770.

33 A. Cassen, Y. Gloaguen, L. Vendier, C. Duhayon, A. Poblador-Bahamonde, C. Raynaud, E. Clot, G. Alcaraz and S. Sabo-Etienne, *Angew. Chem.*, 2014, **126**, 7699–7703; *Angew. Chem., Int. Ed.*, 2014, **53**, 7569–7573.

34 K. D. Hesp, F. O. Kannemann, M. A. Rankin, R. McDonald, M. J. Ferguson and M. Stradiotto, *Inorg. Chem.*, 2011, **50**, 2431–2444.

35 (*a*) J. Brugos, J. A. Cabeza, P. García-Álvarez, A. R. Kennedy, E. Pérez-Carreño and J. F. Van der Maelen, *Inorg. Chem.*, 2016, **55**, 8905–8912; (*b*) J. Brugos, J. A. Cabeza, P. García-Álvarez, E. Pérez-Carreño and J. F. Van der Maelen, *Dalton Trans.*, 2017, **46**, 4009–4017; (*c*) J. F. Van der Maelen, J. Brugos, P. García-Álvarez and J. A. Cabeza, *J. Mol. Struct.*, 2020, **1201**, 12717.

36 K. Smith, A. Pelter and Z. Jin, *Angew. Chem.*, 1994, **106**, 913–914; *Angew. Chem. Int. Ed. Engl.*, 1994, **33**, 851–853.

37 (*a*) G. Alcaraz, U. Helmstedt, E. Clot, L. Vendier and S. Sabo-Etienne, *J. Am. Chem. Soc.*, 2008, **130**, 12878–12879; (*b*) C. S. MacNeil, S.-J. Hsiang and P. G. Hayes, *Chem. Commun.*, 2020, **56**, 12323–12326.

38 M. A. Rankin, K. D. Hesp, G. Schatte, R. McDonald and M. Stradiotto, *Dalton Trans.*, 2009, 4756–4765.